Journal of Materials Chemistry A

PAPER

Cite this: J. Mater. Chem. A, 2014, 2, 15582

Branched CNT@SnO_2 nanorods@carbon hierarchical heterostructures for lithium ion batteries with high reversibility and rate capability†

Shuai Chen, Yuelong Xin, Yiyang Zhou, Feng Zhang, Yurong Ma, Henghui Zhou* and Limin Qi*

Received 24th June 2014
Accepted 22nd July 2014

DOI: 10.1039/c4ta03218g

www.rsc.org/MaterialsA

A novel hierarchical heterostructure consisting of carbon-coated SnO_2 mesocrystalline nanorods radially aligned on carbon nanotubes (CNTs) was designed and fabricated by a two-step growth process. SnO_2 nanorods were first grown directly on CNTs through a facile solvothermal reaction, which were subsequently coated with a thin layer of carbon to form a branched CNT@SnO_2@carbon sandwich-type heterostructure. When used as an anode material in lithium ion batteries, the branched CNT@SnO_2@C heterostructures exhibited highly reversible lithium storage behavior and excellent rate capability. The reversible capacity of the CNT@SnO_2@C heterostructure reached 984 mA h g^{-1} at a current density of 720 mA g^{-1}, and retained 590 mA h g^{-1} at 3.6 A g^{-1} and 420 mA h g^{-1} at 7.2 A g^{-1}. This superior performance might be ascribed to the improved mechanical capability and high loading content of SnO_2 of the branched architecture, the good electrical conductivity of the CNT backbones and the carbon layer, and the high electrochemical reactivity of the 1D mesocrystalline SnO_2 nanorods.

Introduction

Lithium ion batteries (LIBs) have become the predominant power source for a wide variety of applications like portable electronics for many years due to their high energy density, long lifespan and high safety.[1–3] Recently, the demand for high-energy and high-power LIBs for fast-charging electronics and electric vehicles is continually increasing; therefore, new anode materials with higher capacity and better rate performance are required to replace the commercially used graphite.[4] SnO_2 is a promising candidate as an anode material in LIBs due to its high theoretical capacity of 782 mA h g^{-1} and appropriate working potential around 0.6 V (*vs.* Li^+/Li).[5–7] However, the practical applications of SnO_2-based electrodes are significantly limited by their poor cycling stability caused by the large volume change (~240%) of SnO_2 during the alloying and dealloying processes.[5,8] Furthermore, the capacity and cycling stability of SnO_2 at high current density are impaired by its low ionic diffusivity and electronic conductivity, which is unfavorable for its applications in high-power devices.

Designing hybrid materials of SnO_2 nanostructures with carbon-based materials with desirable structures to buffer the volume change and improve the conductivity and ion diffusion is a promising strategy to overcome these disadvantages.[9–12] Carbon nanotubes (CNTs) are a useful material in LIBs due to their excellent conductivity and mechanical properties.[13,14] There have been some reports on the heterostructures of CNTs and SnO_2 nanoparticles[15–20] or nanosheets,[21] and CNT@SnO_2@C sandwich-structured nanocables,[22–25] which exhibited improved cycling stability in LIBs. For the growth of SnO_2 nanocrystals on the surface of CNTs, initial treatment of CNTs with HNO_3 or polyvinylpyrrolidone (PVP) are normally needed to modify the chemically inert surface of CNTs.[15–17,20,21] Generally, these methods lead to relatively low SnO_2 contents in the hybrid materials and poor contact between the active materials and conductive carbon black due to the limited growth of SnO_2, thus impairing the total capacities and rate capabilities of these heterostructures. Notably, one-dimensional (1D) nanostructures have shown great potential in improving the rate performance of nanostructured electrodes because of their high surface area, good conductivity and high mechanical strength.[26–28] For example, the carbon-coated α-Fe_2O_3 hollow nanohorns grown on CNTs exhibited significantly enhanced cycling stability and rate performance.[29] Therefore, the growth of 1D nanostructures on CNTs would be able to both improve the loading mass of SnO_2 and enhance the contact with carbon blacks and electrolyte. However, it is still a challenge to grow SnO_2 1D nanostructures directly on CNTs using the available methods.[15–17,20,21] Moreover, it is noteworthy that mesocrystals,

Beijing National Laboratory for Molecular Sciences, State Key Laboratory for Structural Chemistry of Unstable and Stable Species, College of Chemistry, Peking University, Beijing 100871, P.R. China. E-mail: henghuizhou@pku.edu.cn; liminqi@pku.edu.cn

† Electronic supplementary information (ESI) available: Additional SEM and TEM images, cycling performance data of different SnO_2-based materials, and Nyquist plots. See DOI: 10.1039/c4ta03218g

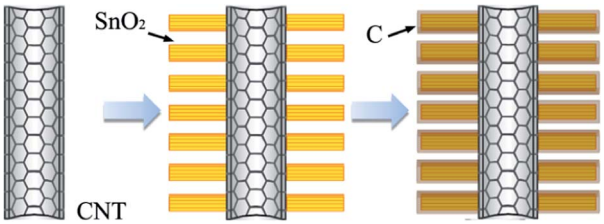

Fig. 1 Schematic illustration of the formation of the branched CNT@SnO_2 nanorods@carbon heterostructures.

which are hierarchical assemblies of crystallographically oriented nanocrystals, are receiving increasing attention as promising electrode materials for high-power LIBs owing to their unique properties of high conductivity and high porosity.[30–32] It is expected that a rational combination of CNTs and SnO_2 1D mesocrystalline nanostructures would lead to LIB anodes with improved rate performance.

Recently, we developed a facile solvothermal method to grow mesocrystalline SnO_2 nanorod arrays on arbitrary inert substrates by controlling the reaction kinetics.[30] These 1D mesocrystalline nanorods can provide good conductivity and short Li ion diffusion lengths, thus exhibiting superior rate performance as an anode material in LIBs. Herein, a novel branched CNT@SnO_2@C hierarchical heterostructure was designed and fabricated using a two-step growth process (Fig. 1). First, a branched CNT@SnO_2 hierarchical heterostructure consisting of SnO_2 mesocrystalline nanorods grown directly on CNTs was synthesized through a kinetically controlled method. The intersecting and highly conductive CNTs construct a three-dimensional (3D) backbone to facilitate the charge transfer, and the branched structure of SnO_2 mesocrystalline nanorods grown on CNTs not only benefits from the good conductivity of the 1D structure and the short ion diffusion length of mesocrystals, but also provides good contact with the electrolyte and carbon black in electrode. Furthermore, a branched CNT@SnO_2@C sandwich-type heterostructure was fabricated by coating a thin layer of carbon on the branched CNT@SnO_2 heterostructure. Owing to the synergy of each constituent in this hybrid structure, the branched heterostructure exhibited a high reversible capacity of 984 mA h g^{-1} at 720 mA g^{-1} and high rate capability (590 mA h g^{-1} at 3.6 A g^{-1} and 420 mA h g^{-1} at 7.2 A g^{-1}) when used as an anode in LIBs.

Experimental section

Synthesis of branched CNT@SnO_2 heterostructures

Branched CNT@SnO_2 heterostructures were solvothermally synthesized in a ternary solvent system using the reported method[30] except for the use of CNTs instead of Ti foil. In a typical synthesis, NaBr (0.275 mmol) was dissolved in 1 mL of deionized (DI) water, and $SnCl_4 \cdot 5H_2O$ (0.2 mmol) was dissolved in 6 mL of glacial acetic acid. These two solutions were then mixed with 1 mL of ethanol and 1 mg of multi-wall carbon nanotubes (110–170 nm × 5–9 μm, Sigma-Aldrich) under ultrasonication. The mixed black sol was transferred to a 25 mL Teflon-lined stainless steel autoclave, which was then heated to 200 °C for 24 h. After the autoclave was cooled to room temperature, the resultant black powder was separated by centrifugation, washed with DI water and ethanol several times, and dried at 70 °C overnight.

Synthesis of branched CNT@SnO_2@C sandwich-type heterostructures

A glucose-derived carbon layer was coated on the branched CNT@SnO_2 heterostructures by a hydrothermal process. 20 mg of the as-prepared branched CNT@SnO_2 heterostructures was dispersed by ultrasonication in 15 mL of 4.7 g L^{-1} aqueous glucose solution. The suspension was transferred to a 25 mL Teflon-lined stainless steel autoclave, which was then heated to 180 °C for 24 h. After the autoclave was cooled to room temperature, the product was separated by centrifugation and washed several times with DI water. After drying at 70 °C, the resultant brown power was carbonized at 500 °C for 2 h under an Ar atmosphere.

Characterization

The heterostructure products were characterized by scanning electron microscopy (SEM, Hitachi S4800, 5 kV), transmission electron microscopy (TEM, FEI Tecnai T20, 200 kV), high-resolution TEM (HRTEM, FEI Tecnai F30, 300 kV), and X-ray diffraction (XRD, Rigaku Dmax-2000, Cu Kα radiation). Thermogravimetric analysis (TGA) was carried out on a Q50 thermoanalyzer with air as the carrier gas at a heating rate of 10 °C min^{-1}. The specific surface area was determined using the Brunauer–Emmett–Teller (BET) method through nitrogen sorption analysis performed on a Micromeritics ASAP 2010 instrument at 77 K.

Electrochemical measurement

Electrochemical charge and discharge tests were performed in 2032 coin cells. The CNT@SnO_2 sample used as a reference in electrochemical tests was calcined at 450 °C for 30 min to remove the residual organic species. The anode mixture was prepared by mixing the active materials, acetylene black, and binder polytetrafluoroethylene (PTFE) at a ratio of 8 : 1 : 1 and was spread on copper foil by use of a blade. Prior to use, the electrode was dried under vacuum at 120 °C overnight before electrochemical tests. The electrode was assembled in an argon-filled glovebox. Li foil was used as the counter electrode, 1 M $LiClO_4$ in propylene carbonate (PC) and dimethyl carbonate (1 : 1 by volume) were used as the electrolyte, and Celgard 2400 was used as the separator. The electrochemical performance was tested by using an ARBIN BT2000 battery test system at room temperature (25 °C). The coin cells were discharged and charged between 2.5 V and 0.05 V at a constant current. The cyclic voltammetry (CV) study was carried out on a CV autolab (Eco Chemie, PGSTAT302N). Electrochemical impedance spectroscopy (EIS) was performed on an electrochemical workstation (Shanghai Chenhua, CHI660D) in the frequency range from 10^{-2} to 10^5 Hz.

Results and discussion

Fig. 2a shows typical SEM images of the multiwalled CNTs used as backbones for the growth of SnO_2 nanorods, which suggests that the CNTs with an average diameter of ~130 nm and lengths of several microns had a rather smooth surface. After the solvothermal growth of mesocrystalline SnO_2 nanorods at 200 °C for 24 h, branched CNT@SnO_2 heterostructures were readily produced. As shown in Fig. 2b, all the CNTs exhibited coarse surfaces with their diameters increasing to around 1 μm, and they intersected with each other. The enlarged SEM image shown in Fig. 2c suggests that the CNTs were uniformly decorated by SnO_2 nanorods with interspaces between each other on the entire surface, showing a novel branched morphology. Fig. 2d shows the cross-section of a fractured CNT@SnO_2 heterostructure, suggesting that the nanorods with a length of 500 nm and an average diameter of 90 nm were grown radially on the surface of the CNTs. The high-magnification SEM image shown in Fig. 2e suggests that each nanorod had a square cross section and the square nanorod was actually composed of a bundle of primary nanorods around 10 nm in width. The TEM image of a typical SnO_2 nanorod clearly shows the primary 1D subunits (Fig. 2f). The corresponding selected-area electron diffraction (SAED) pattern exhibits the single-crystalline diffraction features of rutile SnO_2, indicating that each nanorod consisting of a bundle of primary nanorods is a single-crystal-like SnO_2 mesocrystal growing along the [001] direction with four lateral facets enclosed by the {110} planes, which is consistent with the mesocrystalline SnO_2 nanorod arrays grown on a Ti substrate.[30] The BET surface area of the branched CNT@SnO_2 heterostructures was measured to be ~9.7 $m^2 g^{-1}$, which was somewhat higher than the theoretical maximum value (~7.1 $m^2 g^{-1}$) of solid tetragonal SnO_2 nanorods (about 90 nm × 90 nm × 500 nm in size) with one end blocked regardless of their close packing, indicating the existence of some interstices between the rod-like subunits of the mesocrystalline nanorods. It is worth mentioning that although branched nanostructures of Fe_2O_3 nanohorns grown on CNTs,[29] $ZnCo_2O_4$ nanowires grown on carbon fibers[33] and $NiCo_2O_4$ nanowires grown on carbon textiles[34] have been reported, this is the first report of branched heterostructures of mesocrystalline oxide nanorods grown on 1D carbon nanostructures.

The growth process of mesocrystalline SnO_2 nanorods on CNTs was investigated by examining the products obtained at an earlier growth stage with a reaction time of 3 h. As shown in Fig. 3a and b, a branched product consisted of small SnO_2 nanorods with a length of 100 nm sparsely grown on CNTs were obtained. Fig. 3c shows an HRTEM image of the nascent CNT@SnO_2 heterostructure, which exhibits a clear interface between CNT and a SnO_2 nanorod. The lattice fringes with spacings of 0.34 nm and 0.26 nm in the dark part correspond to the (110) and (101) planes of the rutile SnO_2, and the lattice fringe with a spacing of 0.34 nm in the light part corresponds to the (002) plane of multiwalled CNTs, suggesting the direct growth of small SnO_2 nanorods on the CNTs. It is noteworthy that the heterogeneous growth of SnO_2 nanocrystals on the chemically inert surface of CNTs may also provide a promising strategy to synthesize heterostructures of SnO_2 and other inert carbon-based materials including graphene.

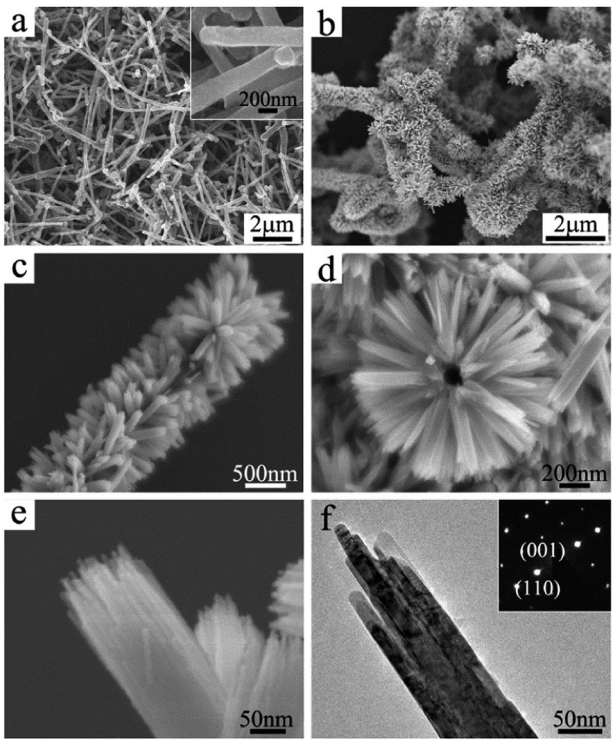

Fig. 2 SEM images of original CNTs (a) and branched CNT@SnO_2 heterostructures (b–d). SEM (e) and TEM (f) images of individual mesocrystalline SnO_2 nanorods grown on CNTs. The inset in (a) shows a high-magnification image, and the inset in (f) is the corresponding SAED pattern.

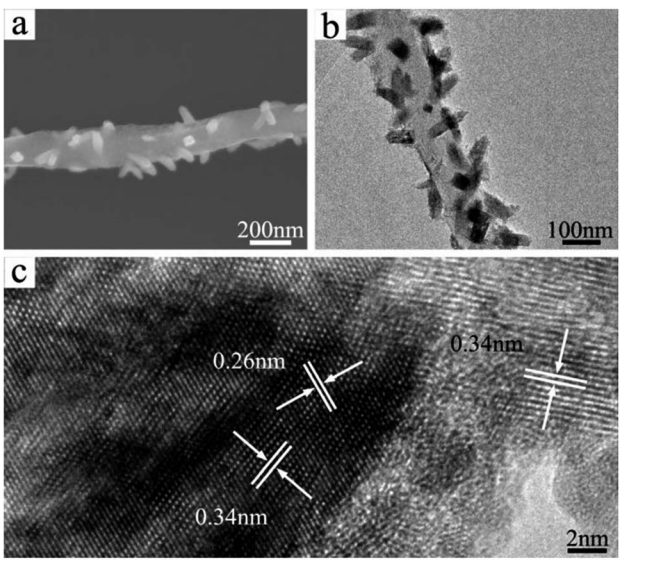

Fig. 3 SEM (a), TEM (b), and HRTEM (c) images of SnO_2 nanorods grown on CNTs after 3 h of a solvothermal reaction.

The amount of CNTs in the solvothermal reaction system had a significant influence on the morphology of the branched CNT@SnO_2 heterostructures (Fig. S1, ESI†). When the amount of CNT in 8 mL of reaction solution containing 25 mM $SnCl_4$ was decreased from 1 mg to 0.5 mg, more nanorods were grown on the surface of CNTs, leading to denser branched structures. When the amount of CNT was increased to 2 mg, sparser branched structures were obtained. When the amount of CNT was further increased to 4 mg, a large number of bare CNTs co-existed with branched CNT@SnO_2 heterostructures, indicating that the presence of excess CNTs was unfavorable for the uniform growth of SnO_2 nanorods. In this ternary solvent system, acetic acid (HAc) and NaBr played key roles in controlling the growth processes of SnO_2. Since HAc is an acidic, coordinating solvent, its concentration largely controlled the hydrolysis rate of Sn(IV), thus affecting the amount of SnO_2 grown on CNTs. As a result, the nanorods grown on CNTs became sparser when the HAc amount added to the reaction system was increased (Fig. S2, ESI†). The amount of NaBr can also affect the density and morphology of the SnO_2 nanorods. Generally, sparser nanorods were achieved at a higher NaBr content, whereas a thick SnO_2 layer consisting of densely packed nanorods were grown around the CNTs in the absence of NaBr (Fig. S3, ESI†), which suggests that the presence of NaBr as an additive significantly influenced the growth of SnO_2 nanorods, probably owing to the adjustment of the ionic strength and the coordination effect of halogen ions.[30]

After the hydrothermal carbonization of glucose in solution, the SnO_2 nanorods grown on CNTs were uniformly coated with a thin layer of polymeric carbon with a thickness of 5 nm (Fig. S4, ESI†). The polymeric carbon-coated CNT@SnO_2 heterostructures were fully carbonized at 500 °C under an Ar atmosphere. There was no apparent change in the morphology of the branched nanostructures after the carbon coating, as shown in Fig. 4a. The TEM characterization shown in Fig. 4b indicated that each SnO_2 nanorod still consisted of a bundle of parallel primary nanorods with diameters between 5 and 10 nm after calcination, and it exhibited a single crystal-like SAED pattern, confirming its mesocrystalline structure. The carbon layer became thinner after complete carbonization with a thickness of ~4 nm (Fig. 4c), probably due to the dehydration carbonization process during calcination. The HRTEM image shown in Fig. 4d shows the outer amorphous carbon coating layer and the inner crystalline SnO_2 with clear lattice fringes with spacings of 0.32 nm and 0.34 nm, corresponding to the (001) and (110) planes of rutile SnO_2, respectively, which is in good agreement with the SAED pattern.

The XRD patterns of the pristine CNTs, the branched CNT@SnO_2 heterostructures, and the branched CNT@SnO_2@C heterostructures are shown in Fig. 5. The pristine CNTs exhibits a sharp reflection corresponding to the (002) plane of graphite (JCPDS no. 25-0284), suggesting the interlayer distance between graphitic layers of multiwalled CNTs. After the kinetically controlled growth of SnO_2 in solution, the reflections of rutile SnO_2 (JCPDS no. 41-1445) appear, which suggests the formation of the CNT@SnO_2 heterostructures. The increased background in the 20–35° region after the growth of SnO_2 suggests the existence of disordered carbon in the CNTs, which was increased after the carbon coating due to the existence of amorphous carbon layer.[35] Due to the 1D structure of SnO_2, a high content of SnO_2 in the branched CNT@SnO_2@C heterostructures could be achieved. The TGA curve of the branched CNT@SnO_2@C heterostructures after full carbonization is shown in Fig. 6 together with those of the hydrothermally produced amorphous carbon and the original CNTs, which

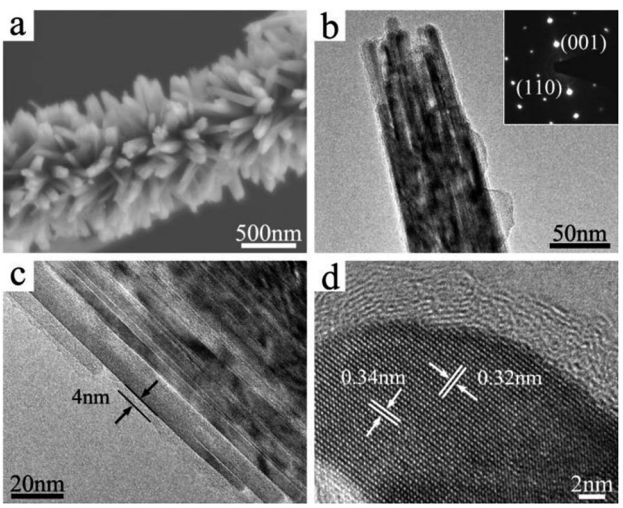

Fig. 4 (a) SEM image of a branched CNT@SnO_2@C hierarchical heterostructure. TEM (b and c) and HRTEM (d) images of a carbon-coated mesocrystalline SnO_2 nanorod. The inset is the corresponding SAED pattern.

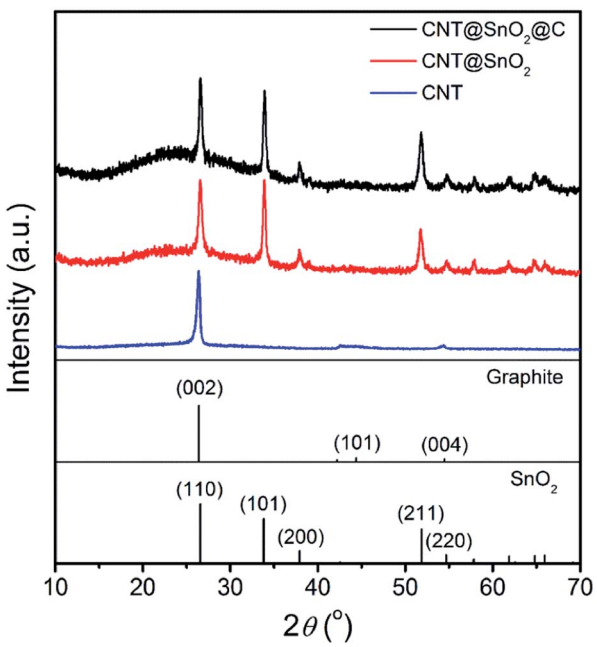

Fig. 5 XRD patterns of CNTs, CNT@SnO_2 heterostructures, and CNT@SnO_2@C heterostructures. The standard XRD patterns of graphite (JCPDS no. 25-0284) and SnO_2 (JCPDS no. 41-1445) are also presented.

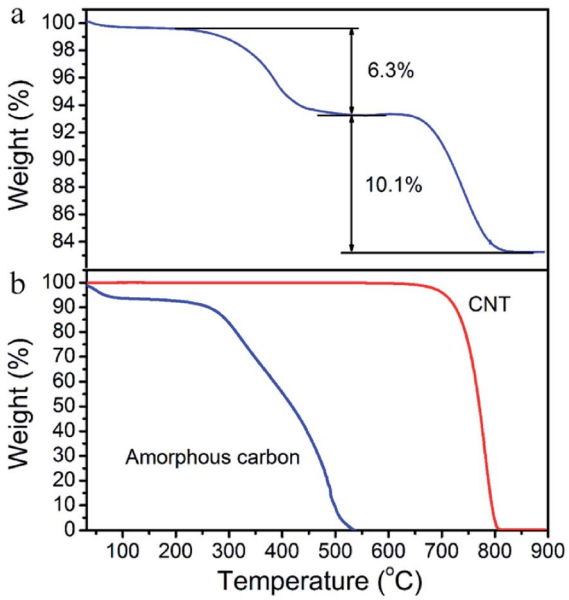

Fig. 6 TGA curves of (a) branched CNT@SnO_2@C heterostructures, and (b) amorphous carbon and original CNTs.

indicates that combustion of the amorphous carbon layers began around 250 °C and was complete around 500 °C, while the combustion of CNTs began around 600 °C and was complete around 800 °C. The contents of the amorphous carbon layer and CNTs were determined to be 6.3% and 10.1% by weight, respectively. Thus, the content of SnO_2 was estimated to be 83.6% by weight, which would be favorable for the overall capacity of the heterostructures as an anode for LIBs. A high theoretical capacity of about 720 mA h g^{-1} can be calculated based on the mass content and theoretical capacity of SnO_2 and carbon (hypothesizing that all carbon-based materials have the same theoretical capacity of 372 mA h g^{-1}).

The lithium storage properties of the obtained branched CNT@SnO_2@C heterostructures as an anode material for LIBs were evaluated using the CNT@SnO_2 heterostructures as a reference. The lithium ion insertion properties of the branched CNT@SnO_2@C heterostructures were first examined by cyclic voltammetry (CV). Fig. 7a shows the CV curves of the branched CNT@SnO_2@C heterostructures for the first three cycles at a scan rate of 0.5 mV s^{-1} in the potential range from 2.5 to 0.05 V (*vs.* Li^+/Li). The electrochemical reactions of SnO_2 in LIBs could be divided into two steps:[5,6]

$$SnO_2 + 4Li^+ + 4e^- \rightarrow Sn + 2Li_2O \quad (1)$$

$$Sn + xLi^+ + xe^- \leftrightarrow Li_xSn\ (0 \le x \le 4.4) \quad (2)$$

In the first reaction (eqn (1)), SnO_2 is irreversibly reduced to metallic Sn and amorphous Li_2O, followed by the highly reversible alloying reaction (eqn (2)), providing a high theoretical capacity of 782 mA h g^{-1} (corresponding to $Li_{4.4}Sn$). Interestingly, two pairs of cathodic/anodic peaks can be clearly observed. The first pair shown at the potentials of 0.05 V and 0.7 V can be attributed to the alloying/dealloying processes of Li_xSn ($0 \le x \le 4.4$), which is generally consistent with normal SnO_2-based materials.[5] The second pair of cathodic/anodic peaks are around 0.65 V and 1.2 V, respectively. The high cathodic peak at 0.65 V observed in the first discharge CV curse can be attributed to the reduction of SnO_2 to metallic tin and amorphous Li_2O, whereas the lower cathodic/anodic peaks around 0.65 V and 1.2 V since the first charge process indicate a reversible transformation between SnO_2 and Sn, which suggests that the second reaction may be partly reversible in this case. Such a reversible lithium ion insertion process can provide additional capacity during the electrochemical reactions, which has been reported for some heterostructures of SnO_2 and carbon-based materials.[11,18,36,37] In the current situation, this phenomenon can be attributed to the enhanced conductivity and good contact between Li_2O and Sn during the discharge/charge processes of the carbon-coated 1D mesocrystalline SnO_2 nanorods grown on CNTs.

The theoretical capacity of the branched CNT@SnO_2@C heterostructures was roughly estimated to be 720 mA h g^{-1} based on the mass contents and the theoretical capacities of SnO_2 and carbon (including both the amorphous carbon layer and CNTs), which were taken to be 782 mA h g^{-1} and 372 mA h g^{-1}, respectively. Fig. 7b shows the charge/discharge voltage profiles of the branched CNT@SnO_2@C heterostructures at a current density of 720 mA g^{-1} (~1 C) with a voltage range from 0.05 to 2.5 V. The initial discharge and charge capacities were found to be 1290 and 829 mA h g^{-1}, respectively, corresponding to a high initial coulombic efficiency of 64.3%. The capacity loss in the first cycle of SnO_2 can be mainly attributed to the irreversible reduction of SnO_2 to Sn and Li_2O (reaction (1)) and the formation of a solid-electrolyte interface (SEI). The discharge/charge capacities slowly increased during the next few cycles and reached the highest reversible capacity of 984 mA h g^{-1} at the fifth cycle. Such a capacity rise during cycling is common for nanostructured metal oxide hybrid electrodes, and may be attributed to the activation of active materials, which improves the lithium ion accessibility in the hybrid during the cycling process, leading to an increased accommodation behavior for lithium.[10,29,38] The capacity of SnO_2 in heterostructures was estimated to be 1069 mA h g^{-1} in this case. Such a high capacity corresponds to the insertion of 6.0 mol Li^+ in 1 mol SnO_2, which is much higher than the theoretical capacity of pure SnO_2 (4.4 mol Li^+ in 1 mol SnO_2). The additional lithium ion storage can be related to the reversible reaction of Li_2O and Sn to SnO_2, which may be caused by interfacial lithium storage in the 1D mesocrystalline structure with small subunits and high surface area, and the enhanced electrochemical activity of carbon-coated SnO_2 grown on highly conductive CNTs, similar to the results reported for other SnO_2-based composite materials in the literature.[11,18,36,37] Interestingly, it has been reported that the CNT@SnO_2@PPy (polypyrrole) coaxial nanocable consisting of SnO_2 nanoparticles exhibited high reversibility with an even higher capacity of 1486 mA h g^{-1} for SnO_2 at a current density of 150 mA g^{-1}.[37] However, due to the low mass content of SnO_2 (55%), the total capacity of the CNT@SnO_2@PPy structures was only 847 mA h g^{-1}, which was lower than the current result

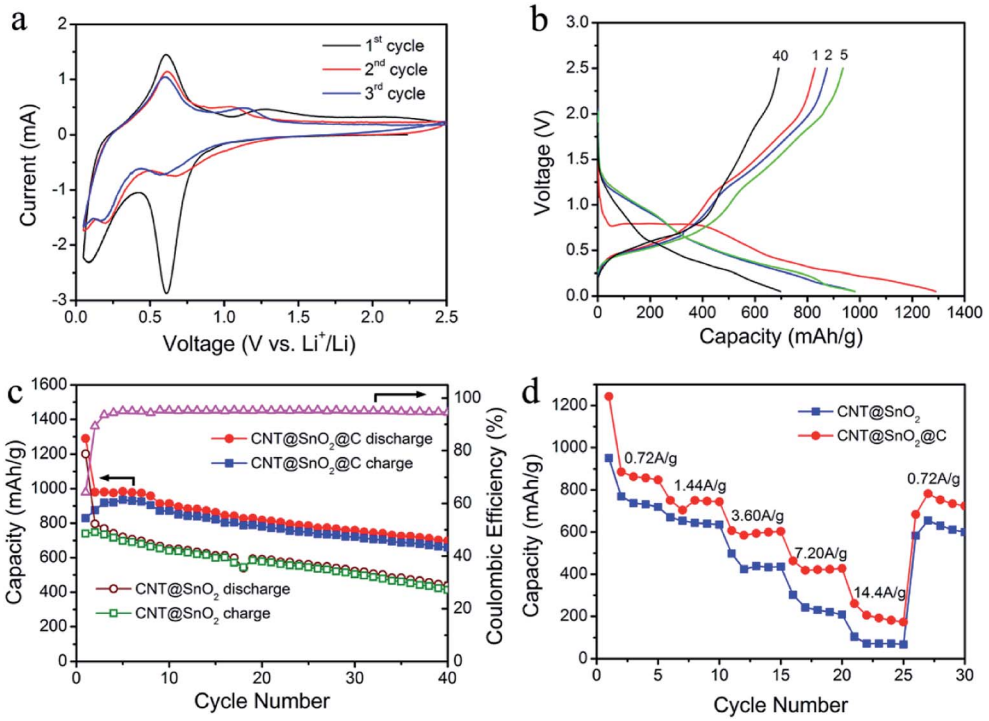

Fig. 7 Electrochemical properties of the branched CNT@SnO_2@C and CNT@SnO_2 heterostructures. (a) Cyclic voltammetry curves from the first to the third cycle at a scan rate of 0.5 mV s^{-1} for branched CNT@SnO_2@C heterostructures. (b) Galvanostatic discharge/charge profiles of branched CNT@SnO_2@C heterostructures. (c) Comparative cycling performance of the branched CNT@SnO_2@C and CNT@SnO_2 heterostructures at a current density of 720 mA g^{-1} together with the coulombic efficiency of the CNT@SnO_2@C heterostructures. (d) Rate capability of branched CNT@SnO_2@C and CNT@SnO_2 heterostructures at different discharge currents.

(984 mA h g^{-1} at 720 mA g^{-1}). This proves the advantages of the branched structures consisting of 1D SnO_2 nanostructure grown on CNTs in terms of the total capacity of the electrode in practical applications. Owing to the supporting effect of the CNTs and the interspaces between the SnO_2 nanorods, the branched CNT@SnO_2@C heterostructures exhibited improved cycling stability. After 40 cycles, the heterostructure retained a reversible capacity of 698 mA h g^{-1}, which is still two times higher than the capacity of graphite. The SEM observations of the CNT@SnO_2@C electrodes before and after 40 cycles at 720 mA g^{-1} suggest that there was no clear deformation and shedding of the electrode film, and only a few small cracks appeared after cycling (Fig. S5a–c, ESI†), confirming the stability of the electrode during cycling. TEM observations of the sample separated from the cycled heterostructure electrode by ultrasonication shows the presence of unbroken nanorod bundles (Fig. S5d, ESI†), suggesting that the hierarchical mesocrystalline nanorods largely retained their original structure during the charge/discharge processes. However, it is difficult to discern whether the nanorods still adhered to the CNTs after cycling since strong sonication was involved in the preparation of the TEM samples.

The cycle performance of the branched CNT@SnO_2@C and CNT@SnO_2 heterostructures at a current density of 720 mA g^{-1} are shown in Fig. 7c. Compared with the branched CNT@SnO_2 heterostructures, the branched CNT@SnO_2@C heterostructures exhibited similar cycling stability but better discharge/charge capacities even with the higher carbon content. In contrast, the mesocrystalline SnO_2 nanorod arrays grown on the Ti substrate[30] synthesized by a similar method showed a capacity between those of CNT@SnO_2 and CNT@SnO_2@C at the initial 20 cycles, followed by rapid capacity loss, possibly due to the weaker strength and conductivity (Fig. S6, ESI†). However, it should be pointed out that the branched CNT@SnO_2@C heterostructures underwent continuous capacity loss after 40 cycles and the capacity decreased gradually to ~116 mA h g^{-1} after 100 cycles (Fig. S7, ESI†). This result suggests that the long-term cycling stability of the CNT@SnO_2@C heterostructures remains to be enhanced by further structural optimization. For example, the cycling performance might be enhanced by designing empty spaces between SnO_2 and the carbon layer.[39] The rate performance of the branched CNT@SnO_2@C and CNT@SnO_2 heterostructures at various discharge/charge rates of 0.72 A g^{-1} to 14.4 A g^{-1} are compared in Fig. 7d. The branched CNT@SnO_2@C heterostructures exhibited excellent rate capability with reversible capacities of 590 mA h g^{-1} at 3.6 A g^{-1} and 420 mA h g^{-1} at 7.2 A g^{-1}. Such high rate capability has not been achieved by the reported SnO_2 nanostructures[40,41] and hybrid materials of SnO_2 and carbon nanomaterials, such as the heterostructures of CNT@SnO_2 nanoparticles,[15,16,18–20] CNT@SnO_2 nanosheets,[21] SnO_2@CNT hybrid structures,[35] graphene nanosheet@SnO_2 nanoparticles,[42] and different carbon-coated SnO_2 nanoparticles grown on carbon-based materials.[22–25,43,44] For example, an ultrafine SnO_2 nanorod retained a capacity of 360 mA h g^{-1}

after 50 cycles at a current density of 0.78 A g^{-1},[40] a carbon nanotube@SnO_2–Au coaxial nanocable exhibited reversible capacities of 467 and 392 mA h g^{-1} at rates of 3.6 A g^{-1} and 7.2 A g^{-1}, respectively,[15] and a sandwiched graphene/SnO_2 nanorod/carbon nanostructure retained a capacity of 540 mA h g^{-1} at a current density of 3 A g^{-1}.[43] The excellent rate capability of the branched CNT@SnO_2@C heterostructures can be largely ascribed to the high conductivity of the CNT backbones, direct pathways for charge transport and short lithium ion diffusion length of the 1D mesocrystalline nanorods, as well as the high mass content of SnO_2 in the heterostructure. It was clearly shown that the rate performance was improved after the carbon coating, indicating that a thin layer of amorphous carbon can improve the conductivity of branched heterostructures and enhance the capacity and rate performance of the electrode. To elucidate the role of the carbon layer in the heterostructures, the electrochemical impedance spectra (Nyquist plots) of the branched CNT@SnO_2 nanostructures with and without the carbon coating were measured (Fig. S8, ESI†). The equivalent electric circuit contains the following: R_s related to the Li^+ transport resistance in the electrolyte, R_f related to the Li^+ migration resistance, R_{ct} related to the charge transfer resistance through the electrode–electrolyte interface, and a Warburg impedance (W), which is associated with Li^+ diffusion in a solid.[45] While the CNT@SnO_2 and CNT@SnO_2@C heterostructures show similar R_s and R_f values, the charge transfer resistance (R_{ct}) of the CNT@SnO_2@C heterostructures (~39 Ω) was much smaller than that of the CNT@SnO_2 heterostructures (~115 Ω), suggesting a considerable improvement in conductivity after the carbon coating.

Thus, each composition in the branched CNT@SnO_2@C heterostructures has provided its unique contribution during the discharge/charge processes in LIBs. First, the highly conductive CNTs formed a backbone in the electrode and provided an interconnected charge pathway, which improved the conductivity and mechanical strength of the electrode. Second, the 1D mesocrystalline SnO_2 nanorods grown on the CNTs exhibited high electrochemical reactivity due to the good conductivity of 1D nanostructures and the short Li ion diffusion length in the small primary subunits. Third, the thin layer of amorphous carbon further improved the conductivity of the whole heterostructures. Moreover, the branched architecture not only provided enough space to buffer volume expansion during cycling and good contact with the conductive carbon blacks, but also brought about a high mass content of SnO_2, thus increasing the total capacity of the heterostructures.

Conclusions

We have developed a facile, two-step growth method for the fabrication of unique, branched CNT@SnO_2 nanorods@carbon hierarchical heterostructures. Branched heterostructures of CNT@SnO_2 were first prepared by growing SnO_2 mesocrystalline nanorods on multiwalled CNTs through a solvothermal method. An amorphous carbon layer was further coated by the hydrothermal carbonization of glucose in solution and subsequent carbonization at 500 °C, leading to the formation of branched CNT@SnO_2@carbon sandwich-type heterostructures. The branched architecture can improve the mechanical strength and conductivity of the heterostructure, and provide a high SnO_2 loading. Benefiting from the synergy of each composition, the CNT@SnO_2@C heterostructures exhibited highly reversible lithium storage behavior and excellent rate capability. The reversible capacity of the CNT@SnO_2@C heterostructure reached 984 mA h g^{-1} at a current density of 720 mA g^{-1}, and retained 590 mA h g^{-1} at 3.6 A g^{-1} and 420 mA h g^{-1} at 7.2 A g^{-1}. The structural design of nanostructured electrodes demonstrated in this work will have implications for the fabrication of new electrode materials for the next-generation LIBs for high-power applications such as fast-charging electronics and electric vehicles. Furthermore, it is expected that this two-step growth method can be extended to the fabrication of various sandwich-type heterostructures consisting of 1D nanostructure arrays of active metal oxides grown on carbon-based substrates with 3D architectures.

Acknowledgements

This work was supported by NSFC (grant no. 21173010, 21073005, and 51121091) and MOST (grant no. 2013CB932601).

Notes and references

1 P. G. Bruce, B. Scrosati and J.-M. Tarascon, *Angew. Chem., Int. Ed.*, 2008, **47**, 2930.
2 K. T. Lee and J. Cho, *Nano Today*, 2011, **6**, 28.
3 M. V. Reddy, G. V. Subba Rao and B. V. R. Chowdari, *Chem. Rev.*, 2013, **113**, 5364.
4 J. Jiang, Y. Li, J. Liu, X. Huang, C. Yuan and X. W. Lou, *Adv. Mater.*, 2012, **24**, 5166.
5 J. S. Chen and X. W. Lou, *Small*, 2013, **9**, 1877.
6 H. Wang and A. L. Rogach, *Chem. Mater.*, 2014, **26**, 123.
7 Q. Zhang, E. Uchaker, S. L. Candelaria and G. Cao, *Chem. Soc. Rev.*, 2013, **42**, 3127.
8 J. Y. Huang, L. Zhong, C. M. Wang, J. P. Sullivan, W. Xu, L. Q. Zhang, S. X. Mao, N. S. Hudak, X. H. Liu, A. Subramanian, H. Fan, L. Qi, A. Kushima and J. Li, *Science*, 2010, **330**, 1515.
9 A. L. M. Reddy, S. R. Gowda, M. M. Shaijumon and P. M. Ajayan, *Adv. Mater.*, 2012, **24**, 5045.
10 X. Zhou, L.-J. Wan and Y.-G. Guo, *Adv. Mater.*, 2013, **25**, 2152–2157.
11 L. Zhang, G. Zhang, H. B. Wu, L. Yu and X. W. Lou, *Adv. Mater.*, 2013, **25**, 2589.
12 L. Q. Zhang, X. H. Liu, Y. Liu, S. Huang, T. Zhu, L. Gui, S. X. Mao, Z. Z. Ye, C. M. Wang, J. P. Sullivan and J. Y. Huang, *ACS Nano*, 2011, **5**, 4800.
13 J. M. Schnorr and T. M. Swager, *Chem. Mater.*, 2010, **23**, 646.
14 B. J. Landi, M. J. Ganter, C. D. Cress, R. A. DiLeo and R. P. Raffaelle, *Energy Environ. Sci.*, 2009, **2**, 638.
15 G. Chen, Z. Wang and D. Xia, *Chem. Mater.*, 2008, **20**, 6951.
16 H.-X. Zhang, C. Feng, Y.-C. Zhai, K.-L. Jiang, Q.-Q. Li and S.-S. Fan, *Adv. Mater.*, 2009, **21**, 2299.

17 Z. Lu and H. Wang, *CrystEngComm*, 2014, **16**, 550.
18 J. Li, Y. Zhao, N. Wang and L. Guan, *Chem. Commun.*, 2011, **47**, 5238.
19 J.-C. Kim, I.-S. Hwang, S.-D. Seo, G.-H. Lee, H.-W. Shim, K.-S. Park and D.-W. Kim, *Nanotechnology*, 2012, **23**, 465402.
20 H. Song, N. Li, H. Cui and C. Wang, *Electrochim. Acta*, 2014, **120**, 46.
21 S. Ding, J. S. Chen and X. W. Lou, *Adv. Funct. Mater.*, 2011, **21**, 4120.
22 P. Wu, N. Du, H. Zhang, J. Yu and D. Yang, *J. Phys. Chem. C*, 2010, **114**, 22535.
23 S. Ding, J. S. Chen and X. W. Lou, *Chem.–Asian J.*, 2011, **6**, 2278.
24 Q. Tian, Z. Zhang, J. Chen, L. Yang and S.-i. Hirano, *J. Power Sources*, 2014, **246**, 587.
25 J. Kong, Z. Liu, Z. Yang, H. R. Tan, S. Xiong, S. Y. Wong, X. Li and X. Lu, *Nanoscale*, 2012, **4**, 525.
26 J. Jiang, Y. Li, J. Liu and X. Huang, *Nanoscale*, 2011, **3**, 45.
27 J. Li, W. Wan, H. Zhou, J. Li and D. Xu, *Chem. Commun.*, 2011, **47**, 3439.
28 J.-Y. Liao, D. Higgins, G. Lui, V. Chabot, X. Xiao and Z. Chen, *Nano Lett.*, 2013, **13**, 5467.
29 Z. Wang, D. Luan, S. Madhavi, Y. Hu and X. W. Lou, *Energy Environ. Sci.*, 2012, **5**, 5252.
30 S. Chen, M. Wang, J. Ye, J. Cai, Y. Ma, H. Zhou and L. Qi, *Nano Res.*, 2013, **6**, 243.
31 Z. Hong, M. Wei, T. Lan and G. Cao, *Nano Energy*, 2012, **1**, 466.
32 J. Ye, W. Liu, J. Cai, S. Chen, X. Zhao, H. Zhou and L. Qi, *J. Am. Chem. Soc.*, 2011, **133**, 933.
33 B. Liu, J. Zhang, X. Wang, G. Chen, D. Chen, C. Zhou and G. Shen, *Nano Lett.*, 2012, **12**, 3005.
34 L. Shen, Q. Che, H. Li and X. Zhang, *Adv. Funct. Mater.*, 2014, **24**, 2630.
35 R. Hu, W. Sun, H. Liu, M. Zeng and M. Zhu, *Nanoscale*, 2013, **5**, 11971.
36 Z. Chen, M. Zhou, Y. Cao, X. Ai, H. Yang and J. Liu, *Adv. Energy Mater.*, 2012, **2**, 95.
37 Y. Zhao, J. Li, N. Wang, C. Wu, G. Dong and L. Guan, *J. Phys. Chem. C*, 2012, **116**, 18612.
38 Z.-S. Wu, Y. Sun, Y.-Z. Tan, S. Yang, X. Feng and K. Müllen, *J. Am. Chem. Soc.*, 2012, **134**, 19532.
39 H. Wu, G. Zheng, N. Liu, T. J. Carney, Y. Yang and Y. Cui, *Nano Lett.*, 2012, **12**, 904.
40 Z. Y. Wang, Z. C. Wang, S. Madhavi and X. W. Lou, *J. Mater. Chem.*, 2012, **22**, 2526.
41 L. Zhang, H. B. Wu, B. Liu and X. W. Lou, *Energy Environ. Sci.*, 2014, **7**, 1013.
42 J. Lin, Z. Peng, C. Xiang, G. Ruan, Z. Yan, D. Natelson and J. M. Tour, *ACS Nano*, 2013, **7**, 6001.
43 D. Wang, J. Yang, X. Li, D. Geng, R. Li, M. Cai, T.-K. Sham and X. Sun, *Energy Environ. Sci.*, 2013, **6**, 2900.
44 J. Cheng, H. Xin, H. Zheng and B. Wang, *J. Power Sources*, 2013, **232**, 152.
45 L. He, C. Wang, X. Yao, R. Ma, H. Wang, P. Chen and K. Zhang, *Carbon*, 2014, **75**, 345.